ORIGINAL PAPER

A dispersion analysis of uniformly high order, interior and boundaries, mimetic finite difference solutions of wave propagation problems

Otilio Rojas[1,2] · Larry Mendoza[3] · Beatriz Otero[4] · Jorge Villamizar[5,6] · Giovanni Calderón[6,7] · Jose E. Castillo[8] · Guillermo Miranda[2]

Abstract

A preliminary stability and dispersion study for wave propagation problems is developed for mimetic finite difference discretizations. The discretization framework corresponds to the fourth-order staggered-grid Castillo-Grone operators that offer a sextuple of free parameters. The parameter-dependent mimetic stencils allow problem discretization at domain boundaries and at the neighbor grid cells. For arbitrary parameter sets, these boundary and near-boundary mimetic stencils are lateral, and we here draw first steps on the parametric dependency of the stability and dispersion properties of such discretizations. As a reference, our analyses also present results based on Castillo-Grone parameters leading to mimetic operators of minimum bandwidth that have been previously applied in similar physical problems. The most interior parameter-dependent mimetic stencils exhibit a specific Toeplitz-like structure, which reduces to the standard central finite difference formula for staggered differentiation at grid interior. Thus, our results apply to the whole discretization grid. The study done for the 1-D problem could be applied to the discretization of a free surface boundary condition along an orthogonal gridline to this boundary.

Keywords Wave propagation · Von Neumann analysis · Numerical dispersion and stability · Mimetic finite differences

Mathematics Subject Classification 65N06

✉ Beatriz Otero
beatriz.otero@upc.edu

Extended author information available on the last page of the article

1 Introduction

Differentiation operators introduce dispersion anomalies on wave propagation simulations due to the discrete sampling of propagation wavelengths across the grid. These errors drive simulation waves to travel at a different speed relative to the continuous propagation velocity. To minimize such errors, the use of high-order operators allows increasing wave sampling and improving numerical accuracy, without densifying numerical meshes. Moreover, tuning of Finite Difference (FD) stencils may reduce such errors to gain fidelity. Now, dispersion analyses at mesh interior based on the Von Neumann method are well established and available in the technical literature (for instance, see Moczo et al. 2007 for a formal discussion in elasticity), but their application at the vicinity of domain boundaries for error quantification is missing. Fourier hypothesis of an infinite or periodic domain is no longer valid, avoiding the development of such analyses.

Similar to alternative volume-discretization schemes, dispersion errors on FD solutions are cumulative with propagation distances, and modern methods use fourth- and higher-order FD discretization stencils in space to suppress these anomalies on traveling wavelengths. For low dispersive simulations, fourth-order FD methods employ discretization meshes that allow sampling the minimum propagation wavelength with at least 6 nodes (Levander 1988; de la Puente et al. 2014). In these cases, the discretization of time derivatives uses the second-order Leapfrog scheme based on central stencils that employs wavefields at two previous time steps. Theoretical support for this commonly used meshing constraint is probably based on the Von Neumann analysis developed in Moczo et al. (2000, 2004) at interior mesh nodes. No guidelines for dispersion analysis are given in these references, to explore the dispersion effects of the lateral discretization approach employed by their well established 3-D FD numerical method when modeling Free Surface (FS) boundary conditions.

In this work, we draw first steps towards a stability and dispersion analysis amenable for FD lateral discretization of linear boundary conditions, i.e., no ghost grid cells are considered. In particular, the fourth-order Staggered-Grid (SG) Mimetic Finite Difference (MFD) Castillo-Grone (CG) operators Gradient denoted as $\mathbf{G}$ and Divergence denoted as $\mathbf{D}$, that offer a sextuple of free parameters $(\alpha_G, \beta_G, \gamma_G)$, and $(\alpha_D, \beta_D, \gamma_D)$, respectively. The dependency of the stability and dispersion properties of our numerical scheme on these parameters is explored in order to experimentally find quasi-optimal parameters. A potential application area of outcomes of this work comprises seismic wave propagation problems, where the FD method on SG has become a flexible and efficient tool for realistic modeling (see again, Moczo et al. 2007).

Here, we limit ourselves to FD discretizations of wave propagation models, where boundary conditions are discretized by lateral FD stencils as given in Castillo and Yasuda (2003) for second order accuracy, and in Castillo et al. (2001), Castillo and Grone (2003) for fourth- and sixth-order calculations. In addition, time integration proceeds under a second-order Leapfrog scheme. In Solano Feo (2017) and Solano-Feo et al. (2016), acoustic waves are modeled by means of a fully mimetic scheme that include the three $\mathbf{D}$, $\mathbf{G}$ and $\mathbf{B}$ operators. In the following works, fourth-order $\mathbf{D}$ and $\mathbf{G}$ have been exclusively used, i.e. the boundary operator $\mathbf{B}$ has been neglected to avoid the limited experimental accuracy to second order, as reported in Blanco et al. (2016).

Non linear rupture problems in elastic media are modeled by Rojas et al. (2008, 2009), using the minimum-bandwidth CG operators, and these authors do not draw conclusions that favor the use of integrations of higher order. In 2-D elastic media, surface Rayleigh wave modeling also benefit from mimetic lateral discretizations and the contribution in Rojas et al. (2014) standouts from previous vacuum based FD treatments. A potential cause of vacuum formulation inaccuracies is the material extrapolation out of the physical domain. Mimetic discretization of boundary conditions based on lateral stencils avoid these type of formulations where ghost points might require field extrapolations beyond boundaries that lacks of physical sense Castillo and Grone (2003).

In addition, results achieved by Rojas et al. (2017) in 1-D propagation scenarios show the reduction of dispersion anomalies thanks to the use of fourth- and higher-order Lax Wendroff temporal corrections. In addition, three-dimensional boundary fitted curvilinear coordinates have allowed the precise MFD implementations of non-flat topographies and bathymetries on deformed SG to model seismic motion on geometrically realistic domains (de la Puente et al. 2014; Shragge and Tapley 2017; Konuk and Shragge 2021; Sethi et al. 2022). As reported, these high-order applications do not explore the contribution of mimetic parameters available in **D** and **G**. To the best of our knowledge, an alternative family of mimetic parameters has been explored in Córdova (2017), where an approximate negative adjoint condition leads to a sextuple that enlarge the Courant-Friedrichs-Lewy (CFL) stability range on 1-D acoustic experiments. The work in Córdova (2017) is an extension of the previous method in Córdova et al. (2016) to model acoustic wave propagation.

The matrix stability analysis of second-order MFD methods for the wave equation and for the diffusion equation, developed in Solano-Feo et al. (2016) and Castillo-Nava and Guevara-Jordan (2023), respectively are insightful on the accuracy properties of these methods. This analysis is mainly based on eigenvalue estimations of the associated matrix to the method discrete formulation which allows CFL bounding, but are not useful to understand dispersion in wave propagation simulations.

This paper is structured as follows. First, we present our MFD SG discretization of the 1-D wave model in Sect. 2, and develop a formal Von Neumann stability and dispersion. Then, we proceed with an intensive parameter exploration to find low dispersive candidates in Sect. 3, which are confirmed by numerical results. Finally, brief conclusions and future guidelines are presented in Sect. 4.

2 Stability and dispersion: 1-D Fourier analysis

Von Neumann based stability and dispersion analysis at mesh interior are well established and available in a well established literature (for instance, Moczo et al. 2007 and Strikwerda 2004). On the contrary, similar studies in the vicinity of domain boundaries for error quantification are missing, mainly because Fourier hypothesis of an infinite domain or function periodicity are no longer valid. In this work, we propose a stability and dispersion analysis amenable for FD lateral discretization of linear boundary conditions. Several FD methods to model elastic wave propagation are derived from the velocity v and stress τ formulation of the wave equation, e.g., Levander (1988),
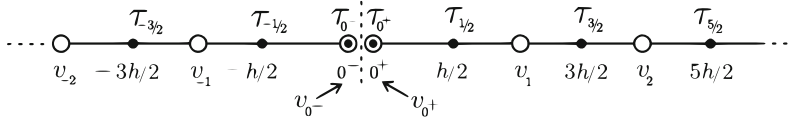
Fig. 1 Discretization of the 1-D velocity-stress wave formulation along a staggered grid

Gao and Keyes (2020), and Sethi et al. (2021). Here, we consider the following 1-D velocity-stress formulation

$$\begin{cases} \rho \dot{v} = \tau_x \\ \dot{\tau} = \mu v_x \end{cases} ; \tag{1}$$

to be solved along an infinite string where an artificial interface is introduced at the point $x = 0$, as illustrated in Fig. 1. Above, ρ represents material density and μ corresponds to a Lame modulus.

We introduce a uniform grid of step $h = x_i - x_{i-1} > 0$ for all i and define the distribution of discrete velocities at nodes x_i, with $i = 0, \pm 1, \pm 2, \ldots, \pm N$, and its cells (elements) are the intervals $[x_{i-1}, x_i]$. The discrete stresses are defined at intermediate centers of the cells given by $x_{i+1/2} = (x_i + x_{i+1})/2$, in addition to boundary stress values at x_0. By using MFD operators, the SG differentiation can be given by $\tau_x \approx \mathbf{G}(\tau_0, \tau_{1/2}, \ldots)^T$ and $v_x \approx \mathbf{D}(v_0, v_1, \ldots)^T$. The parametric definition of $\mathbf{G}$ and $\mathbf{D}$ has been developed in Castillo et al. (2001) and Castillo and Grone (2003), and recently the textbook Castillo and Miranda (2013) spends its appendix J to present a comprehensive formulation of these operators. Fourth-order $\mathbf{G}$ and $\mathbf{D}$ are given by

$$\mathbf{G} = \begin{pmatrix} g_{11} & g_{12} & g_{13} & g_{14} & g_{15} & g_{16} & 0 & \cdots \\ \frac{16}{105} - \frac{128}{35}\alpha_G & -\frac{31}{24} + 9\alpha_G & \frac{29}{24} - 12\alpha_G & -\frac{3}{40} + \frac{54}{5}\alpha_G & \frac{1}{168} - \frac{36}{7}\alpha_G & \alpha_G & 0 & \cdots \\ -\frac{128}{35}\beta_G & \frac{1}{24} + 9\beta_G & -\frac{27}{24} - 12\beta_G & \frac{27}{24} + \frac{54}{5}\beta_G & -\frac{1}{24} - \frac{36}{7}\beta_G & \beta_G & 0 & \cdots \\ -\frac{16}{105} - \frac{128}{35}\gamma_G & \frac{3}{8} + 9\gamma_G & -\frac{11}{24} - 12\gamma_G & -\frac{27}{40} + \frac{54}{5}\gamma_G & \frac{51}{56} - \frac{36}{7}\gamma_G & \gamma_G & 0 & \cdots \\ 0 & 0 & 0 & \frac{1}{24} & -\frac{27}{24} & \frac{27}{24} & -\frac{1}{24} & \cdots \\ \vdots & \vdots & \vdots & \vdots & & & & \end{pmatrix} \tag{2}$$

where
$g_{11} = -\frac{124832}{42735} + \frac{16512}{1295}\alpha_G + \frac{18816}{2035}\beta_G + \frac{13696}{1295}\gamma_G$, $\quad g_{12} = \frac{10789}{3256} - \frac{1161}{37}\alpha_G - \frac{9261}{407}\beta_G - \frac{963}{37}\gamma_G$,
$g_{13} = -\frac{421}{9768} + \frac{1548}{37}\alpha_G + \frac{12348}{407}\beta_G + \frac{1284}{37}\gamma_G$, $\quad g_{14} = -\frac{12189}{16280} - \frac{6966}{185}\alpha_G - \frac{55566}{2035}\beta_G - \frac{5778}{185}\gamma_G$,
$g_{15} = \frac{11789}{22792} + \frac{4644}{259}\alpha_G + \frac{5292}{407}\beta_G + \frac{3852}{259}\gamma_G$ $\quad g_{16} = -\frac{48}{407} - \frac{129}{37}\alpha_G - \frac{1029}{407}\beta_G - \frac{107}{37}\gamma_G$.
Likewise, the three-parameter family of fourth-order accurate divergence $\mathbf{D}$ reads

$$\mathbf{D} = \begin{pmatrix} d_{11} & d_{12} & d_{13} & d_{14} & d_{15} & d_{16} & 0 \cdots \\ \frac{1}{24} - \alpha_D & -\frac{27}{24} + 5\alpha_D & \frac{27}{24} - 10\alpha_D & -\frac{1}{24} + 10\alpha_D & -5\alpha_D & \alpha_D & 0 \cdots \\ -\beta_D & \frac{1}{24} + 5\beta_D & -\frac{27}{24} - 10\beta_D & \frac{27}{25} + 10\beta_D & -\frac{1}{24} - 5\beta_D & \beta_D & 0 \cdots \\ -\frac{1}{24} - \gamma_D & \frac{5}{24} + 5\gamma_D & -\frac{3}{8} - 10\gamma_D & -\frac{17}{24} + 10\gamma_D & \frac{11}{12} - 5\gamma_D & \gamma_D & 0 \cdots \\ 0 & 0 & 0 & \frac{1}{24} & -\frac{27}{24} & \frac{27}{24} & -\frac{1}{24} \cdots \\ 0 & 0 & 0 & 0 & \frac{1}{24} & -\frac{27}{24} & \frac{27}{24} \cdots \\ 0 & 0 & 0 & 0 & 0 & \frac{1}{24} & -\frac{27}{24} \cdots \\ 0 & 0 & 0 & 0 & 0 & 0 & \frac{1}{24} \cdots \\ \vdots & \vdots & \vdots & \vdots & & & \end{pmatrix} \quad (3)$$

where
$$d_{11} = -\frac{6851}{7788} + \frac{39}{59}\alpha_D + \frac{675}{649}\beta_D + \frac{551}{649}\gamma_D, \quad d_{12} = \frac{8153}{15576} - \frac{195}{59}\alpha_D - \frac{3375}{649}\beta_D - \frac{2755}{649}\gamma_D,$$

$$d_{13} = \frac{3867}{5192} + \frac{390}{59}\alpha_D + \frac{6750}{649}\beta_D + \frac{5510}{649}\gamma_D, \quad d_{14} = -\frac{9005}{15576} - \frac{390}{59}\alpha_D - \frac{6750}{649}\beta_D - \frac{5510}{649}\gamma_D$$

$$d_{15} = \frac{3529}{15576} + \frac{195}{50}\alpha_D + \frac{3375}{649}\beta_D + \frac{2755}{649}\gamma_D, \quad d_{16} = -\frac{24}{649} - \frac{39}{59}\alpha_D - \frac{675}{649}\beta_D - \frac{551}{649}\gamma_D.$$

Notice that the left upper block of matrices G and D in Eqs. (2) and (3) may become a full 4×6 matrix for arbitrary values of parameters $\alpha_G, \beta_G, \gamma_G, \alpha_D, \beta_D,$ and γ_D. In the special case of $(\alpha_G, \beta_G, \gamma_G, \alpha_D, \beta_D, \gamma_D) = (0, 0, -1/24, 0, 0, -1/24)$, the bandwidth of such upper blocks reduces and we call the resulting mimetic G and D as the minimum bandwidth operators. Namely,

$$\mathbf{G} = \begin{pmatrix} -\frac{47888}{14245} & \frac{1790}{407} & -\frac{14545}{9768} & \frac{8997}{16280} & -\frac{2335}{22792} & \frac{25}{9768} & 0 \cdots \\ \frac{16}{105} & -\frac{31}{24} & \frac{29}{24} & -\frac{3}{40} & -\frac{1}{168} & 0 & 0 \cdots \\ 0 & \frac{1}{24} & -\frac{27}{24} & \frac{27}{24} & -\frac{1}{24} & 0 & 0 \cdots \\ 0 & 0 & \frac{1}{24} & -\frac{27}{24} & \frac{27}{24} & -\frac{1}{24} & 0 \cdots \\ \vdots & \vdots & \vdots & \vdots & & & \end{pmatrix} \quad (4)$$

and

$$\mathbf{D} = \begin{pmatrix} -\frac{4751}{5192} & \frac{909}{1298} & \frac{6091}{15576} & -\frac{1165}{5192} & \frac{129}{2596} & -\frac{25}{15576} & 0 \cdots \\ \frac{1}{24} & -\frac{27}{24} & \frac{27}{24} & -\frac{1}{24} & 0 & 0 & 0 \cdots \\ 0 & \frac{1}{24} & -\frac{27}{24} & \frac{27}{24} & -\frac{1}{24} & 0 & 0 \cdots \\ 0 & 0 & \frac{1}{24} & -\frac{27}{24} & \frac{27}{24} & -\frac{1}{24} & 0 \cdots \\ \vdots & \vdots & \vdots & \vdots & & & \end{pmatrix} \quad (5)$$

The resulting minimum bandwidth G and D operators given above have been used to implement boundary conditions for elastic wave propagation in Rojas et al. (2008, 2009, 2014, 2017). In addition, Shragge and Tapley (2017) employs D for similar purposes on elastic-acoustic problems.

The interface continuity conditions at $x = 0$ are $v(0^-, t) = v(0^+, t)$, and $\tau(0^-, t) = \tau(0^+, t)$. By considering time differentiation of the velocity continuity in addition to the wave equation, the continuity of τ_x across the interface proceeds. This condition is discretized by using the operator G, i.e., the lateral FD stencil defined by the first G row. Thus, upon lateral discretization of $\tau_x\big]_{0^+}^m$ and $\tau_x\big]_{0^-}^m$, we obtain

$$
\begin{aligned}
\tau_0^m = -\frac{1}{2g_{11}}\Big\{ &g_{12}\Big(\tau_{1/2}^m + \tau_{-1/2}^m\Big) + g_{13}\Big(\tau_{3/2}^m + \tau_{-3/2}^m\Big) + g_{14}\Big(\tau_{5/2}^m + \tau_{-5/2}^m\Big) \\
&+g_{15}\Big(\tau_{7/2}^m + \tau_{-7/2}^m\Big) + g_{16}\Big(\tau_{9/2}^m + \tau_{-9/2}^m\Big)\Big\}
\end{aligned}
\tag{6}
$$

Next, we state our numerical scheme based on a staggered Leapfrog time integration and a MFD spatial discretization

$$
\begin{cases}
v^{m+1/2} - v^{m-1/2} = \left(\frac{\Delta t}{\rho h}\right) G\tau^m \\
\tau^{m+1} - \tau^m = \left(\frac{\Delta t \mu}{h}\right) D v^{m+1/2}
\end{cases}
\tag{7}
$$

In the following, we develop a Von Neumann analysis of this scheme to quantify the stability and dispersion dependence on the parameters $\alpha_G, \beta_G, \gamma_G, \alpha_D, \beta_D$, and γ_D. The discrete equation for velocity updating at any node x_j for $j = \pm 1, \pm 2, \pm 3, \pm 4$ is simply given by

$$
v_{j-1}^{m+1/2} - v_{j-1}^{m-1/2} = \left(\frac{\Delta t}{\rho h}\right)\Big\{ g_{j1}\tau_0^m + g_{j2}\tau_{1/2}^m + g_{j3}\tau_{3/2}^m + g_{j4}\tau_{5/2}^m + g_{j5}\tau_{7/2}^m + g_{j6}\tau_{9/2}^m \Big\}
\tag{8}
$$

This equation can be rewritten by substituting τ_0 by using condition (6) and the consistency FD property $g_{j2} = -g_{j1} - g_{j3} \cdots - g_{j6}$, in the form

$$
v_{j-1}^{m+1/2} - v_{j-1}^{m-1/2} = \left(\frac{\Delta t}{\rho h}\right)\Big\{ \Sigma_{\exp}^{\tau,j} + \Sigma_{\cos}^{\tau,j} \Big\}
\tag{9}
$$

where
$$
\begin{aligned}
\Sigma_{\exp}^{\tau,j} = \Big\{ &-g_{j1}\tau_{1/2} + g_{j3}\Big(\tau_{3/2}^m - \tau_{1/2}^m\Big) + g_{j4}\Big(\tau_{5/2}^m - \tau_{1/2}^m\Big) + g_{j5}\Big(\tau_{7/2}^m - \tau_{1/2}^m\Big) \\
&+g_{j6}\Big(\tau_{9/2}^m - \tau_{1/2}^m\Big)\Big\}
\end{aligned}
$$

$$
\begin{aligned}
\Sigma_{\cos}^{\tau,j} = \Big\{ &-f_{j2}\Big(\tau_{1/2}^m + \tau_{-1/2}^m\Big) - f_{j3}\Big(\tau_{3/2}^m + \tau_{-3/2}^m\Big) - f_{j4}\Big(\tau_{5/2}^m + \tau_{-5/2}^m\Big) \\
&-f_{j5}\Big(\tau_{7/2}^m + \tau_{-7/2}^m\Big) - f_{j6}\Big(\tau_{9/2}^m + \tau_{-9/2}^m\Big)\Big\}
\end{aligned}
$$

for coefficients f_{jl} defined as $f_{jl} = g_{j,1}g_{1,l}/2g_{1,1}$, with $l = 2, 3, \ldots, 6$.

In a similar way, the Leapfrog updating equation for near-boundary stresses can be written after using the consistency equation on **D** stencils as

$$\tau_J^{m+1} - \tau_J^m = \left(\frac{\mu \Delta t}{h}\right) \left\{ \Sigma_{\exp}^{v,j} \right\} \tag{10}$$

where $J = \pm 1/2, \pm 3/2, \pm 5/2, \pm 7/2$, and

$$\Sigma_{\exp}^{v,j} = \left\{ d_{j2}\left(v_1^{m+1/2} - v_0^{m+1/2}\right) + d_{j3}\left(v_2^{m+1/2} - v_0^{m+1/2}\right) + d_{j4}\left(v_3^{m+1/2} - v_0^{m+1/2}\right) \right.$$
$$\left. + d_{j5}\left(v_4^{m+1/2} - v_0^{m+1/2}\right) + d_{j6}\left(v_5^{m+1/2} - v_0^{m+1/2}\right) \right\}$$

Our numerical scheme results after coupling these two discrete Eqs. (9) and (10) for tuples $(j, J) = \pm(0, 1/2), \pm(1, 3/2), \pm(2, 5/2), \pm(3, 7/2)$, i.e., $j = J - 1/2$.

Next, we proceed with our Von Neumann analysis by assuming the following discrete harmonic solutions

$$\tau_J^m = B e^{\mathrm{i}(-\omega m \Delta t + kJh)}, \qquad J = \pm 1/2, \pm 3/2, \pm 5/2, \ldots \tag{11a}$$

$$v_j^{m \pm 1/2} = A e^{\mathrm{i}\left(-\omega(m \pm 1/2)\Delta t + kjh\right)}, \quad j = 0, \pm 1, \pm 2, \ldots, \quad m = 0, 1, 2, \ldots, \tag{11b}$$

where ω is the angular frequency, i.e., $\omega = 2\pi f$, being f frequency, and k is wavenumber, also known as the spatial frequency of a wave. Coefficients A and B are arbitrary wave amplitudes. A basic physical relation, between k and the wavelength λ is $k = 2\pi/\lambda$. Now, according to the Nyquist theorem the numerical grid must sample each propagation wavelength with at least two nodes. Therefore, $0 \leq h \leq \lambda/2$. If we use the relation between k and λ, then we get

$$0 \leq h \leq \pi/k$$

which is equivalent to $0 \leq kh \leq \pi$. Thus, we define the angle $\theta = kh$ and then $\theta \in [0, \pi]$. The concepts of wavenumber and wavelength, along with Nyquist theorem applications can be found in textbooks, such as Marks II (2009), Stein and Wysession (2009). By introducing,

$$z^m = e^{-\mathrm{i}m\omega\Delta t}$$

the harmonic solutions (11a) and (11b) can be written as

$$\tau_J^m = B z^m e^{\mathrm{i}J\theta} \tag{12}$$

$$v_j^{m \pm 1/2} = A z^{m+1/2} e^{\mathrm{i}j\theta} \tag{13}$$

The next step is writing the right-hand side terms of Eqs. (9) and (10) considering the above expressions for τ_j^m and $v_j^{m\pm1/2}$. First, we have

$$
\begin{aligned}
\tau_J^m - \tau_{1/2}^m &= Bz^m \left(e^{iJ\theta} - e^{i\theta/2} \right) \\
&= Bz^m e^{i\theta/2} \left(e^{i(J-1/2)\theta} - 1 \right)
\end{aligned}
\tag{14}
$$

for $J = 3/2, 5/2, 7/2, 9/2$ that allows writing

$$
\Sigma_{\exp}^{\tau,j} = Bz^m \Delta_{\exp}^{\tau,j}
\tag{15}
$$

for

$$
\Delta_{\exp}^{\tau,j} = e^{i\theta/2} \left(-g_{j1} + g_{j3}\left(e^{i\theta} - 1\right) + g_{j4}\left(e^{2i\theta} - 1\right) + g_{j5}\left(e^{3i\theta} - 1\right) + g_{j6}\left(e^{4i\theta} - 1\right) \right)
$$

Second, please note that

$$
\tau_J^m + \tau_{-J}^m = Bz^m \left(e^{iJ\theta} + e^{-iJ\theta} \right) = 2Bz^m \cos(J\theta)
$$

for $J = 1/2, 3/2, 5/2, 7/2, 9/2$ that lead us to

$$
\Sigma_{\cos}^{\tau,j} = 2Bz^m \Delta_{\cos}^{\tau,j}
\tag{16}
$$

for

$$
\Delta_{\cos}^{\tau,j} = \left\langle -f_{j2} \cos\left(\tfrac{1}{2}\theta\right) - f_{j3} \cos\left(\tfrac{3}{2}\theta\right) - f_{j4} \cos\left(\tfrac{5}{2}\theta\right) - f_{j5} \cos\left(\tfrac{7}{2}\theta\right) - f_{j6} \cos\left(\tfrac{9}{2}\theta\right) \right\rangle
$$

In addition, we have

$$
v_j^{m+1/2} - v_0^{m+1/2} = Az^{m+1/2} \left(e^{ij\theta} - 1 \right)
$$

for $j = 1, 2, 3, 4, 5$ that allows writing

$$
\Sigma_{\exp}^{v,J} = Az^{m+1/2} \Delta_{\exp}^{v,J}
\tag{17}
$$

for

$$
\Delta_{\exp}^{v,J} = d_{j2}\left(e^{i\theta} - 1\right) + d_{j3}\left(e^{2i\theta} - 1\right) + d_{j4}\left(e^{3i\theta} - 1\right) + d_{j5}\left(e^{4i\theta} - 1\right) + d_{j6}\left(e^{5i\theta} - 1\right)
$$

where $j = J - 1/2$.

Now, we reduce the left-hand side of Leapfrog Eqs. (9) and (10) to the case of solutions (12) and (13). First,

$$v_{j-1}^{m+1/2} - v_{j-1}^{m-1} = A z^m \left(z^{1/2} - z^{-1/2} \right) e^{i(j-1)\theta}$$

and after noting that $z^{1/2} - z^{-1/2} = (-2i) \sin\left(\frac{\omega \Delta t}{2}\right)$
the term above equals to

$$v_{j-1}^{m+1/2} - v_{j-1}^{m-1/2} = (-2i) A z^m e^{i(j-1)\theta} \sin\left(\frac{\omega \Delta t}{2}\right) \tag{18}$$

Similarly, in the case of equation (10), we have

$$\tau_J^{m+1} - \tau_J^m = B z^m e^{iJ\theta} (z-1) \tag{19}$$

Finally, by using Eqs. (15), (16) and (18), the first Leapfrog equation (9) can be expressed in the form

$$A \sin\left(\frac{\omega \Delta t}{2}\right) = \frac{1}{2}(Bi)\left(\frac{\Delta t}{\rho h}\right) e^{-i(j-1)\theta} \left\{ \Delta_{\exp}^{\tau,j} + 2\Delta_{\cos}^{\tau,j} \right\}, \tag{20}$$

In a similar manner, we use Eqs. (17) and (19) to write the second Leapfrog equation (10) as

$$B z^m e^{iJ\theta} (z-1) = \left(\frac{\mu \Delta t}{h}\right) A z^{m+1/2} \Delta_{\exp}^v$$

that simplifies to

$$B e^{iJ\theta} \left(z^{1/2} - z^{-1/2} \right) = \left(\frac{\mu \Delta t}{h}\right) A \Delta_{\exp}^v$$

and finally leads to

$$B \sin\left(\frac{\omega \Delta t}{2}\right) = \frac{1}{2}iA\left(\frac{\mu \Delta t}{h}\right) e^{iJ\theta} \left\{ \Delta_{\exp}^{v,J} \right\}, \tag{21}$$

where $J = 1/2, 3/2, 5/2, 7/2$.

Then, we consider the product of previous Eqs. (20) and (21) that simplifies to

$$\sin^2\left(\frac{\omega \Delta t}{2}\right) = -\frac{1}{4} p^2 \Omega_{j,J} \Delta_{\exp}^{v,J} \left\{ \Delta_{\exp}^{\tau,j} + \Delta_{\cos}^{\tau,j} \right\}. \tag{22}$$

Above $\Omega_{j,J} = e^{-i(j+J-1)}$ and $p = c\Delta t/h$ is the CFL ratio that controls numerical stability in time-dependent problems Strikwerda (2004). Now, we next

state the necessary stability condition

$$\frac{1}{2} p \left| \Omega_{j,J} \Delta_{\exp}^{v,J} \left(\Delta_{\exp}^{\tau,j} + \Delta_{\cos}^{\tau,j} \right) \right|^{1/2} \leq 1 \tag{23}$$

The limiting CFL is given by the maximum $p_{\max}$ value that allows bounding by 1 the right hand side of Eq. (23). In this way, there exist real solutions for ω, and the model solutions (11a) and (11b) are harmonic in time, and therefore bounded. Next, we state the numerical wave speed $c_{num} = \omega/k$ after obtaining the numerical angular frequency ω from equation (22), i.e.,

$$c_{num} = \frac{2}{k\Delta t} \arcsin \left(\frac{p}{2} \sqrt{ -\mathrm{Re} \left(\Omega_{j,J} \Delta_{\exp}^{v,J} \left(\Delta_{\exp}^{\tau,j} + \Delta_{\cos}^{\tau,j} \right) \right) } \right). \tag{24}$$

Above only the real part of the right hand side of equation (22) intervenes in the definition of c_{num} (see, for instance, Bohlen and Wittkamp 2016). We further develop this equation by writing the square root argument in terms of quantities

$$\Gamma_{j,J} = \left(\mathrm{Re} \left(\Omega_{j,J} \right) \mathrm{Re} \left(\Delta_{\exp}^{v,J} \right) - \mathrm{Im} \left(\Omega_{j,J} \right) \mathrm{Im} \left(\Delta_{\exp}^{v,J} \right) \right) \left(\mathrm{Re} \left(\Delta_{\exp}^{\tau,j} \right) + \Delta_{\cos}^{\tau,j} \right) \tag{25}$$

and

$$\Upsilon_{j,J} = - \left(\mathrm{Re} \left(\Omega_{j,J} \right) \mathrm{Im} \left(\Delta_{\exp}^{v,J} \right) + \mathrm{Im} \left(\Omega_{j,J} \right) \mathrm{Re} \left(\Delta_{\exp}^{v,J} \right) \right) \mathrm{Im} \left(\Delta_{\exp}^{v,j} \right) \tag{26}$$

The ratio c_{num}/c measures the numerical dispersion of the MFD method, being $c = \sqrt{\mu/\rho}$ the material wave speed. Below, we denote this ratio as $\mathscr{D}_{j,J}^{(4)}$ to emphasize the couple staggered nodes (j, J), and corresponding mimetic stencils, involved in definitions of $\Sigma_{\exp}^{\tau,j}$, $\Sigma_{\exp}^{v,J}$, and $\Sigma_{\cos}^{\tau,j}$. In addition, the exponent 4 denotes the accuracy order of such stencils. In Appendix A, we present dispersion curves for the case of second-order operators G and D, which are denoted as $\mathscr{D}_{j,J}^{(2)}$.

It is worth noting, that the expression in Eq. (22) can be rewritten by using the trigonometric identity

$$\sin^2(\theta) = \frac{1}{2}(1 - \cos(2\theta)) \tag{27}$$

in the following way

$$-\Omega_{j,J} \Delta_{\exp}^{v,J} \left\{ \Delta_{\exp}^{\tau,j} + \Delta_{\cos}^{\tau,j} \right\} = \frac{2}{p^2}(1 - \cos(\omega\Delta t)). \tag{28}$$

Given that $1 - \cos(\omega\Delta t) \geq 0$ for $\omega \in \mathbb{R}$, we have that

$$-\mathrm{Re} \left(\Omega_{j,J} \Delta_{\exp}^{v,J} \left(\Delta_{\exp}^{\tau,j} + \Delta_{\cos}^{\tau,j} \right) \right) \geq 0, \tag{29}$$

and the Eq. (24) is well defined yielding real solutions for c_{num}.

Finally, the dispersion curves are stated after dividing Eq. (24) by c and considering $k = 2\pi/\lambda$ in the form

$$\mathscr{D}_{j,J}^{(4)}(\overline{h}; p) = \frac{1}{p\pi\overline{h}} \arcsin\left(\frac{p}{2}\sqrt{\Gamma_{j,J} + \Upsilon_{j,J}}\right), \qquad (30)$$

for $0 \le \overline{h} \le \frac{1}{2}$ and $p \le p_{\max}$. On wave propagation problems, numerical dispersion $\mathscr{D}$ depends on the grid resolution $\overline{h}$, defined as $\overline{h} = h/\lambda$. This scaled spatial step represents the number of grid points sampling each simulation wavelength λ, where $\overline{h} \to 0$ corresponds to high grid resolution, and $\overline{h} = \frac{1}{2}$ is the limiting Nyquist sampling. This term is typically referred to as points per wavelength. Equation (30) also expresses the explicit dispersion dependence on the CFL number p. For validation, we repeat this analysis using the standard central FD second- and fourth-order stencils to reconstruct the dispersion and stability properties of traditional schemes, as discussed in Moczo et al. (2004) and Levander (1988). Our results replicate these references as described in Appendix A. In the next section, we undertake a computational search of mimetic parameters that minimize $\mathscr{D}$ and report corresponding $p_{\max}$ values.

3 Stability and dispersion: results

Given its various applications, we first report on the minimum bandwidth parameter set $(\alpha_G, \beta_G, \gamma_G, \alpha_D, \beta_D, \gamma_D) = (0, 0, -1/24, 0, 0, -1/24)$. Figure 2 depicts dispersion curves on the boundary stencil tuple $(\upsilon_0, \tau_{1/2})$, while Figs. 3, 4 and 5 show dispersion curves on the three near-boundary stencil tuples $(\upsilon_1, \tau_{3/2})$, $(\upsilon_2, \tau_{5/2})$ and $(\upsilon_3, \tau_{7/2})$, respectively. MFD discretization leading to the stencil tuples $(\upsilon_2, \tau_{5/2})$ and $(\upsilon_3, \tau_{7/2})$ only involves the central staggered stencil given in rows 3 and 4 of matrices G and D in Eqs. (4) and (5). Thus, Figs. 3 and 4 replicate published results by Levander (1988) (see, Appendix A). The four values of the CFL number p allow illustrating its effect on the dispersion curves shown in different colors, being errors higher as p grows and grid resolution reduces.

In every figure, the largest p value corresponds to the stability limit $p_{\max}$ of each scheme stencil tuple, which is given in Table 1. We obtain these $p_{\max}$ values by considering the angle partition $\theta = 0 : \pi/200 : \pi$ and finding the maximum value $M(\theta)$ of the squared root term in (23). Thus, we have that $p_{\max} = 2/M$. Notice that the two lateral stencil tuples $(\upsilon_0, \tau_{1/2})$ and $(\upsilon_1, \tau_{3/2})$ lead to distinct dispersion curves, especially the curves in Fig. 2, that shows a supersonic behavior where simulation waves travel faster than the material wave speed, i.e, $c_{num} > c$ for all p values. In the rest of these figures, we find curves in the subsonic regime, i.e, $c_{num} < c$, with observed transitions from super to subsonic regimes in the cases of $p < p_{\max}$.

Concerning the stability limits given in Table 1, note that the two lateral stencil tuples $(\upsilon_0, \tau_{1/2})$ and $(\upsilon_1, \tau_{3/2})$ impose lower CFL limits with respect to the interior stencil couples, in 15% ($0.73/0.857 \sim 0.852$) and 5% ($0.814/0.857 \sim 0.95$), respectively. Thus, the first lateral stencil tuple strongly limits the global stability of the MFD scheme.
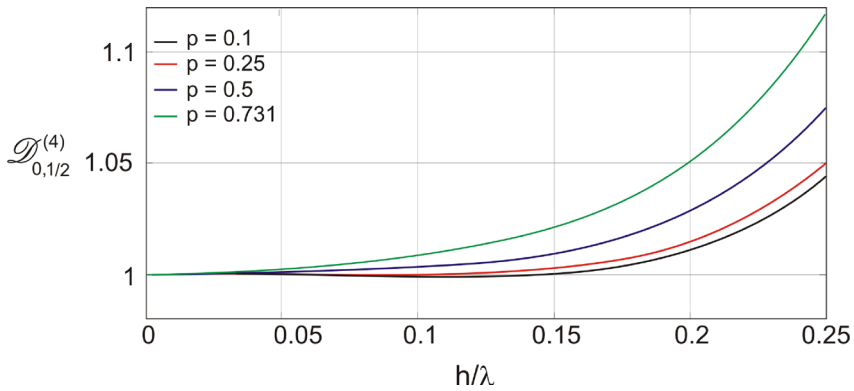
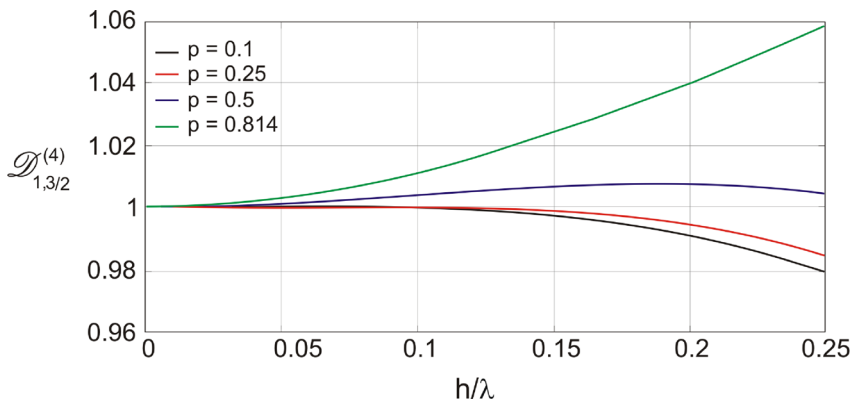**Fig. 2** Dispersion curves of the stencil tuple $(v_0, \tau_{1/2})$ for the minimum bandwidth parameter set

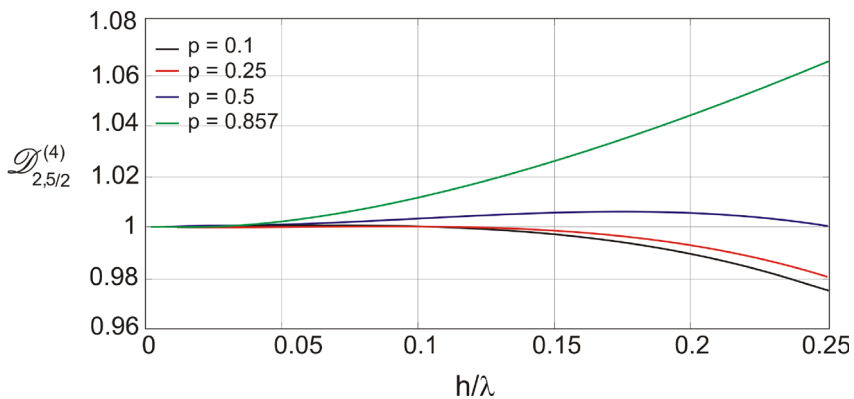**Fig. 3** Dispersion curves of the stencil tuple $(v_1, \tau_{3/2})$ for the minimum bandwidth parameter set

Fig. 4 Dispersion curves of the stencil tuple $(v_2, \tau_{5/2})$ for the minimum bandwidth parameter set
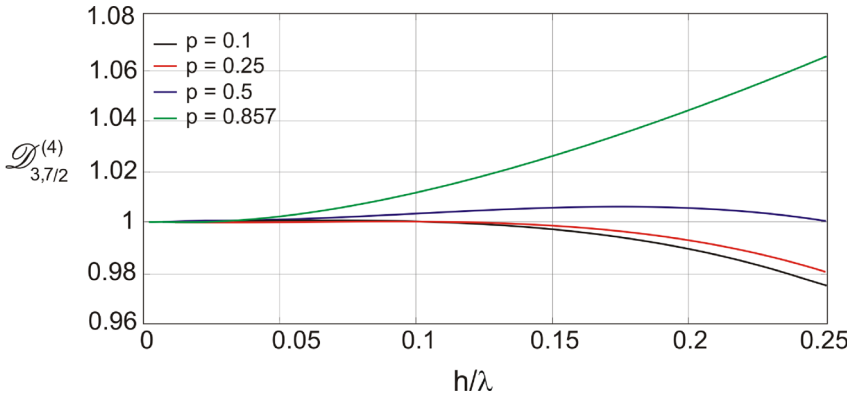
Fig. 5 Dispersion curves of the stencil tuple $(v_3, \tau_{7/2})$ for the minimum bandwidth parameter set

Table 1 Maximum CFL imposed by the discretization at boundary

Operators	Order	$\left(v_0, \tau_{1/2}\right)$	$\left(v_1, \tau_{3/2}\right)$	$\left(v_2, \tau_{5/2}\right)$	$\left(v_3, \tau_{7/2}\right)$	$p_{\max}$ [**CFL**]
Min bandwidth	4th	0.73	0.81	0.85	0.85	0.73
Low dispersive	4th	0.64	0.83	0.85	0.85	0.64

To study the method stability dependence on the six mimetic parameters, we vary each parameter in the interval $[-1, 1]$ using a sampling step of $\frac{1}{100}$ and numerically find $p_{\max}$, as explained above. These evaluations are performed for each stencil couple $(v_0, \tau_{1/2})$, $(v_1, \tau_{3/2})$, $(v_2, \tau_{5/2})$ and $(v_3, \tau_{7/2})$, given the dependency of Eq. (23) on the stencil indexes (j, J) that define a discretization grid cell. In all these cases, we obtain lower $p_{\max}$ values for the boundary-cell stencil $(v_0, \tau_{1/2})$. Thus, this border grid cell also limits the global stability of the MFD scheme for these more general parameter cases, as observed for the minimum bandwidth set. As an illustration, Figs. 6, 7, and 8, depict results for the parameter tuples $(\alpha_G, 0, 0, \alpha_D, 0, 0)$, $(0, \beta_G, 0, 0, \beta_D, 0)$ and $(0, 0, \gamma_G, 0, 0, \gamma_D)$, respectively. As one can see, $p_{\max}$ drastically reduces as any of the mimetic parameters approaches either 1 or -1. The $p_{\max}$ decay as any parameter goes to ± 1 is a general behavior regardless of the values of the other parameters. Notice that a small $p_{\max}$ value translates into a large number of simulation iterations, however, our minimization of numerical dispersion considers all the available samples in $(-1, 1)$ for each mimetic parameter. This numerical exploration of the parameter space lasts for 5 days in an Intel Core i7 processor with 16 GB of RAM running MATLAB R2023b.

In order to quantify dispersion, we introduce the following error metric

$$\epsilon_{j,J} = \int_0^{0.25} \left(\mathscr{D}_{j,J}^{(4)}(\overline{h}; p_{\max}) - 1\right)^2 d\overline{h} \tag{31}$$

where $\mathscr{D}_{j,J}^{(4)}$ is given by Eq. (30), and stencil indexes (j, J) denote its dependence on the discretization grid cell. We use the available evaluations of $\Omega_{j,J}$, $\Delta_{\exp}^{v,J}$, $\Delta_{\exp}^{\tau,j}$, and

Fig. 6 Maximum CFL values for variation of α_G and α_D parameters in the interval $[-1, 1]$
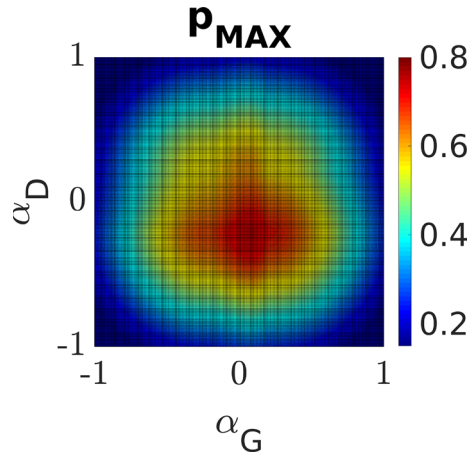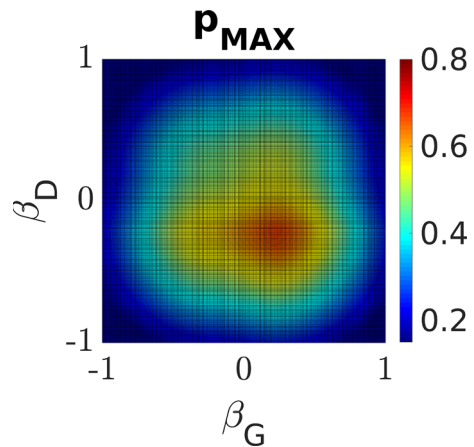

Fig. 7 Maximum CFL values for variation of β_G and β_D parameters in the interval $[-1, 1]$

$\Delta_{\cos}^{\tau,j}$ from the previous p_{max} study, and compute $\epsilon_{j,J}$ for each stencil couple $(\upsilon_0, \tau_{1/2})$, $(\upsilon_1, \tau_{3/2})$, $(\upsilon_2, \tau_{5/2})$ and $(\upsilon_3, \tau_{7/2})$. First, we observe higher ϵ values in the case of the boundary-cell stencil tuple $(\upsilon_0, \tau_{1/2})$, for all parameters samples. Second, we obtain lower values of $\epsilon_{0,1/2}$ for the parameter tuples $(\alpha_G,0,\gamma_G,\alpha_D,0,\gamma_D)$, for each parameter $\alpha_G, \alpha_D, \gamma_G$ and γ_D taking values in the interval $[-0.1, 0.1]$. Thus, we further refine the four-dimensional parameter space associated with $(\alpha_G,\alpha_D,\gamma_G,\gamma_D)$ and find the sample with the lowest dispersion that corresponds to $(-1/40,0,-1/24,119/5494,0,-1/24)$ (after expressing parameter values as fractions). This low dispersive parameter sample is shown as a filled dot in Fig. 9a, b, where $\epsilon_{0,1/2}$ and p_{max} are depicted for variations of α_G and α_D in the interval $\left[\frac{-1}{24}, \frac{1}{24}\right]$. Finally, the maximum stability CFL values imposed by this low dispersive parameter sample for each stencil couple are given in Table 1. The boundary-cell stencil limits the stability of the MFD scheme at $p_{max} = 0.64$.

Next, we depict the dispersion curves of the low dispersive parameter set $(\alpha_G, \beta_G, \gamma_G, \alpha_D, \beta_D, \gamma_D)=(-1/40, 0, -1/24, 119/5494, 0, -1/24)$ corresponding to the boundary and near-boundary grid cells in Figs. 10 and 11, respectively. In these plots, we present

Fig. 8 Maximum CFL values for variation of γ_G and γ_D parameters in the interval $[-1, 1]$
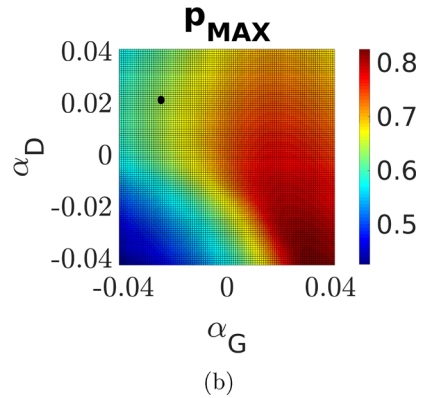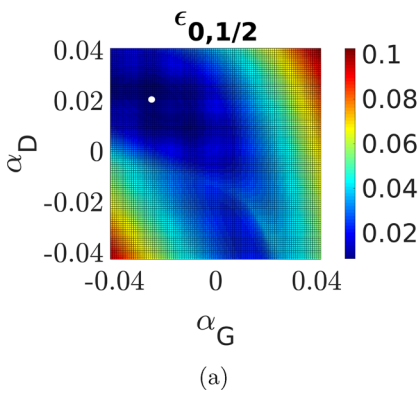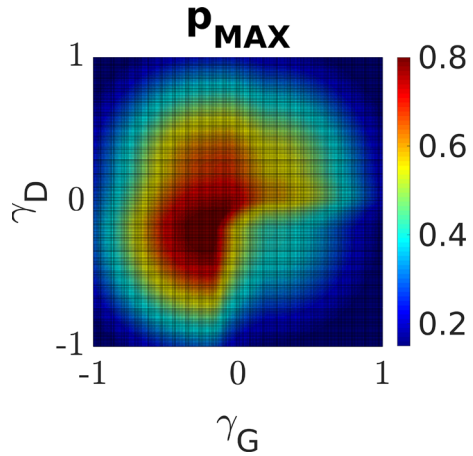

Fig. 9 a Dispersion errors for variation of α_G and α_D parameters in the interval $\left[\frac{-1}{24}, \frac{1}{24}\right]$. **b** Maximum CFL values for variation of α_G and α_D parameters in the interval $\left[\frac{-1}{24}, \frac{1}{24}\right]$. The low dispersive sample $(\alpha_G, \beta_G, \gamma_G, \alpha_D, \beta_D, \gamma_D) = (-1/40, 0, -1/24, 119/5494, 0, -1/24)$ is shown with a filled dot

the curves for reference CFL values of $p = 0.1, 0.25, 0.5$ used in Figs. 2 and 3 to facilitate a direct qualitative comparison. In addition, Figs. 10 and 11 also show curves associated with the particular maximum CFL $p_{\max} = 0.65$. In the case of Fig. 10, dispersion curves adopt a subsonic behavior as the grid resolution reduces, i.e., for $\bar{h} \to \frac{1}{2}$. Alternatively, the dispersion curves in Fig. 2 consistently follow a supersonic behavior as $\bar{h}$ increases.

In the particular case of the dispersion curve associated with $p_{\max}$ in Fig. 10 (the green curve), it experiences a transition from supersonic to subsonic regimes along $\bar{h}$, and approaches 0.95 as $\bar{h}$ goes to 0.25. This represents a maximum dispersion error of 5% when the MFD method performs at $p_{\max}$. The dispersion curve corresponding to $p_{\max}$ in Fig. 2, quantifies an error larger than 10% at the minimum grid resolution of $\bar{h} = 0.25$. On the other hand, Figs. 3 and 11 show a similar dispersion behavior by the near-boundary stencil $(v_1, \tau_{3/2})$, for both minimum bandwidth and low dispersive parameter
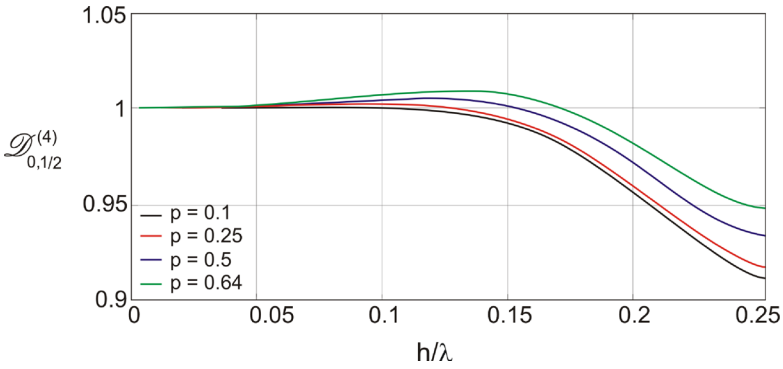
Fig. 10 Dispersion curves of the stencil tuple $(v_0, \tau_{1/2})$ for the low dispersive parameter set
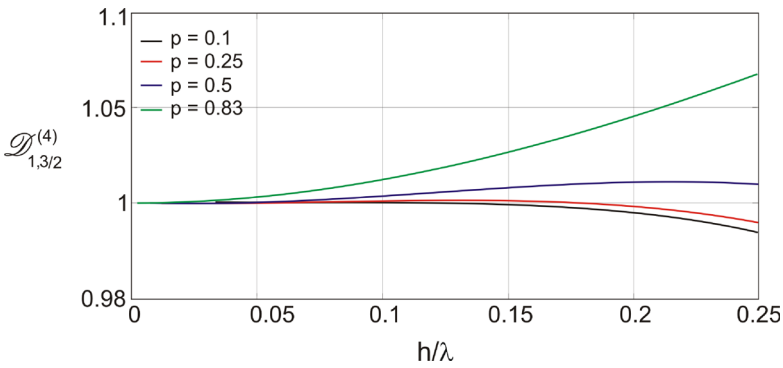

Fig. 11 Dispersion curves of the stencil tuple $(v_1, \tau_{3/2})$ for the low dispersive parameter set

sets. $(\alpha_G, \beta_G, \gamma_G, \alpha_D, \beta_D, \gamma_D) = (-1/40, 0, -1/24, 119/5494, 0, -1/24)$ corresponding to the boundary and near-boundary grid cells in Figs. 10 and 11, respectively. In these plots, we present the curves for reference CFL values of $p = 0.1, 0.25, 0.5$ used in Figs. 2 and 3 to facilitate a direct qualitative comparison as mentioned before.

To compare the performance of the low dispersive and the minimum bandwidth parameter sets, we simulate the propagation of a 1-D Gaussian pulse and allow multiple edge reflections for error accumulation. Results are shown in Fig. 12. It is noteworthy, that the low dispersive candidate operates at maximum CFL condition, while simulation using the minimum bandwidth parameter set employs a less restrictive CFL (by 5%). Dispersion anomalies are lower in the solution of our proposed candidate. That is, the amplitude of the preceding and trailing wave oscillations around the main real pulse are lower in the case of the low dispersive parameters. In addition, the spatial shift between the peak amplitudes of the simulation pulse and their corresponding peak exact values is slightly higher for the solution using the minimum bandwidth parameters.
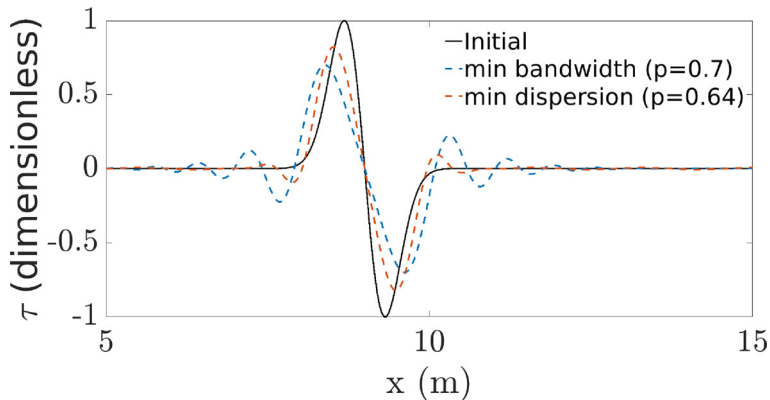
Fig. 12 1-D propagation of a Gaussian pulse

4 Conclusions

We present a Von Neumman stability and dispersion analysis of a fourth-order staggered-grid MFD method that allows finding mimetic parameters of low dispersion. Stability limits of the four different stencils that conform the method are also established and the lateral discretization at the boundary point is the most restrictive one. Although this fact is well known, our analytical finding serves as formal proof. To validate this analysis, we perform 1-D numerical simulations and show the low dispersive performance of the proposed parameters. In addition, our analysis replicates reference results when applied to conventional central stencils. This study also covers the zero stress boundary conditions along a grid orthogonal direction, being relevant to 2-D and 3-D acoustic wave propagation problems.

As a future work, a stability matrix analysis can be added to our current analysis. In addition, the quasi adjoint parameter given by Córdova et al. (2017) can be also considered. Rigorous Fourier stability and dispersion analysis of acoustic and elastic wave equations is cumbersome in 2-D and 3-D (for instance, see Sethi et al. (2021)), and we also plan on extending our current work to undertake such analysis following the methodology in Moczo et al. (2000).

Declarations

Conflict of interest The authors declare that they have no conflict of interest.

Appendix A: Central nodes and second-order case

Here, we show results for interior nodes as a way to verify the previous formulation. The SG distribution of discrete wavefields is shown in Fig. 13. The fourth order central FD stencil is given by $c_0 = h^{-1}\frac{27}{24}$, $c_1 = -h^{-1}\frac{1}{24}$ applied at interior nodes and the resulting Leapfrog method (7) in the Fourier domain simply becomes

$$A \sin\left(\tfrac{\omega \Delta t}{2}\right) = B\left(-\tfrac{1}{2i}\right)\left(\tfrac{\Delta t}{\rho h}\right) e^{i(J-j)\theta} \Delta^\tau, \tag{A-1}$$

$$B \sin\left(\tfrac{\omega \Delta t}{2}\right) = A\left(-\tfrac{1}{2i}\right)\left(\tfrac{\mu \Delta t}{h}\right) e^{i(j-J)\theta} \Delta^\upsilon. \tag{A-2}$$

By combining the previous Eqs. (A-1) and (A-2) result

$$\sin^2\left(\tfrac{\omega \Delta t}{2}\right) = -\tfrac{1}{4}p^2\{\Delta^\tau \cdot \Delta^\upsilon\} \tag{A-3}$$

where

$$\Delta^\tau \cdot \Delta^\upsilon = \left\{ c_0\left(1 - e^{-i\theta}\right) + c_1 e^{i\theta}\left(1 - e^{-3i\theta}\right) \right\}. \tag{A-4}$$

The right hand side simplifies to

$$\Delta^\tau \cdot \Delta^\upsilon = \left\{ c_0^2(1 - \cos\theta) + 2C_0 c_1(\cos\theta - \cos 2\theta) + c_1^2(1 - \cos 3\theta) \right\}. \tag{A-5}$$

By simply using $|\cos\theta| \le 1$, the stability relationship establishes that

$$\left| \sin\left(\tfrac{\omega \Delta t}{2}\right)\right| \le p\big(|c_0| + |c_1|\big) \le 1$$

and leads to the simpler stability constraint

$$p \le \frac{1}{|c_0| + |c_1|} = \frac{1}{\frac{27}{24} + \frac{1}{24}} = \frac{6}{7} \approx 0.8571428571\ldots$$

This result is derived in Fornberg (1988), where the dispersion relation is

$$\mathscr{D}^{(2)}(\overline{h}; p) = \frac{1}{\pi\, p\overline{h}} \arcsin\left(\tfrac{1}{\sqrt{2}} p\{ c_0^2(1 - \cos\theta) + 2c_0 c_1(\cos\theta - \cos 2\theta) + c_1^2(1 - \cos 3\theta)\}\right),$$
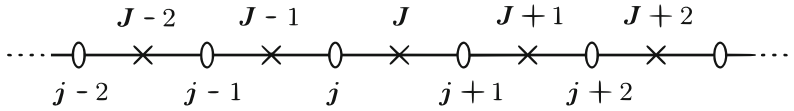
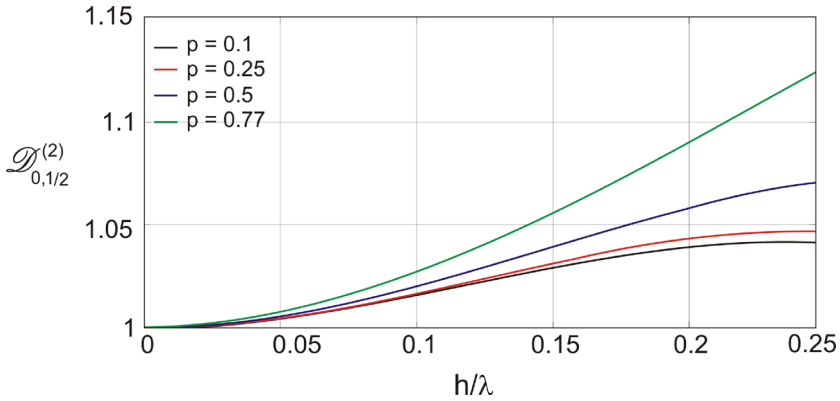**Fig. 13** Interior nodes along a staggered grid

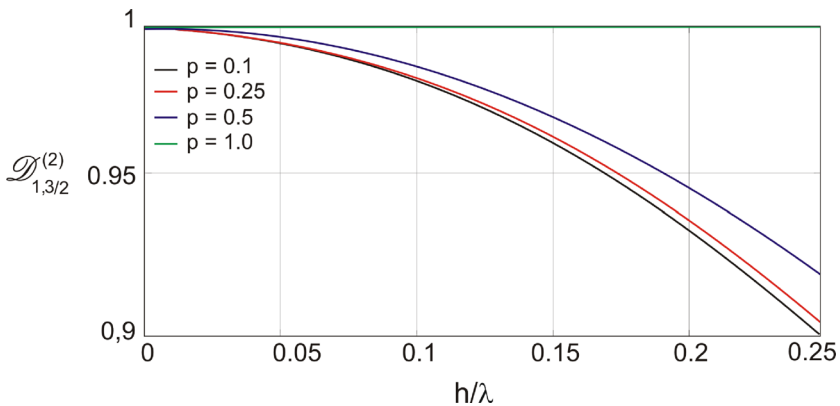**Fig. 14** Dispersion curves for lateral second order discretization

Fig. 15 Dispersion curves for central second order discretization

with $0 \le \overline{h} \le \frac{1}{2}$. Now, if we interchange notation c_o by c_1 and c_1 by $-c_2$ to correct minor typographical errors in Levander (1988), our results match his original ones.

Finally, we show the lateral second order dispersion curves for different CFL values in Fig. 14. These curves are obtained by replacing four order G and D operators in Eqs. (6) and (7) by their second order counterparts explicitly given in Castillo and Yasuda (2003). Notice a supersonic stage that differs from the subsonic behavior of the central discretization as shown in the well known Fig. 15 (found in Moczo et al. (2004), for instance). In this context, numerical super(sub)sonic propagation refers that simulation wavelengths travel faster(slower) than the material wave speed.

References

Blanco, J., Rojas, O., Chacon, C., Guevara-Jordan, J., Castillo, J.: Tensor formulation of 3-D mimetic finite differences and applications to elliptic problems. Electron. Trans. Numer. Anal. ETNA **45**, 457–475 (2016)

Bohlen, T., Wittkamp, F.: Three-dimensional viscoelastic time-domain finite-difference seismic modelling using the staggered Adams–Bashforth time integrator. Geophys. J. Int. **204**(3), 1781–1788 (2016)

Castillo, J.E., Grone, R.D.: A matrix analysis approach to higher-order approximations for divergence and gradients satisfying a global conservation law. SIAM J. Matrix Anal. Appl. **25**(1), 128–142 (2003). https://doi.org/10.1137/S0895479801398025

Castillo, J.E., Miranda, G.F.: Mimetic Discretization Methods. CRC Press, Boca Raton (2013)

Castillo, J.E., Yasuda, M.: A comparison of two matrix operator formulations for mimetic divergence and gradient discretizations. In: International Conference on Parallel and Distributed Processing Techniques and Applications vol. III, pp. 1281–1285 (2003)

Castillo, J.E., Hyman, J.M., Shashkov, M., Steinberg, S.: Fourth- and sixth-order conservative finite difference approximations of the divergence and gradient. Appl. Numer. Math. **37**(1), 171–187 (2001). https://doi.org/10.1016/S0168-9274(00)00033-7

Castillo-Nava, M., Guevara-Jordan, J.: A new analysis of an implicit mimetic scheme for the heat equation. J. Appl. Math. Phys. **11**, 841–857 (2023). https://doi.org/10.4236/jamp.2023.113056

Córdova, L.: Diferencias finitas compactas nodales y centro distribuidas aplicadas a la simulación de ondas acústicas. Ph.D. Thesis, Universidad Central de Venezuela (2017). http://hdl.handle.net/10872/20192

Córdova, L.J., Rojas, O., Otero, B., Castillo, J.: Compact finite difference modeling of 2-D acoustic wave propagation. J. Comput. Appl. Math. **295**(C), 83–91 (2016). https://doi.org/10.1016/j.cam.2015.01.040

Fornberg, B.: Generation of finite difference formulas on arbitrarily spaced grids. Math. Comput. **51**(184), 699–706 (1988). https://doi.org/10.2307/2008770

Gao, L., Keyes, D.: Explicit coupling of acoustic and elastic wave propagation in finite-difference simulations. Geophysics **85**(5), 293–308 (2020). https://doi.org/10.1190/geo2019-0566.1

Konuk, T., Shragge, J.: Tensorial elastodynamics for anisotropic media. Geophysics **86**, 293–303 (2021). https://doi.org/10.1190/geo2020-0156.1

Levander, A.R.: Fourth-order finite-difference P-SV seismograms. Geophysics **53**(11), 1425–1436 (1988). https://doi.org/10.1190/1.1442422

Marks, R.J., II.: Handbook of Fourier Analysis & Its Applications. Oxford University Press, Oxford (2009). https://doi.org/10.1093/oso/9780195335927.001.0001

Moczo, P., Kristek, J., Bystrický, E.: Stability and grid dispersion of the P-SV 4th-order staggered-grid finite-difference schemes. Stud. Geophys. Geod. **44**, 381–402 (2000). https://doi.org/10.1023/A:1022112620994

Moczo, P., Kristek, J., Halada, L.: The finite-difference method for seismologists: an introduction, pp. 1–150 (2004)

Moczo, P., Kristek, J., Galis, M., Pazak, P., Balazovjech, M.: The finite-difference and finite-element modeling of seismic wave propagation and earthquake motion. Acta Phys. Slov. **57**, 177–406 (2007). https://doi.org/10.2478/V10155-010-0084-X

Puente, J., Ferrer, M., Hanzich, M., Castillo, J.E., Cela, J.M.: Mimetic seismic wave modeling including topography on deformed staggered grids. Geophysics **79**(3), 125–141 (2014). https://doi.org/10.1190/geo2013-0371.1

Rojas, O., Day, S., Castillo, J., Dalguer, L.A.: Modelling of rupture propagation using high-order mimetic finite differences. Geophys. J. Int. **172**(2), 631–650 (2008). https://doi.org/10.1111/j.1365-246X.2007.03651.x

Rojas, O., Dunham, E.M., Day, S.M., Dalguer, L.A., Castillo, J.E.: Finite difference modelling of rupture propagation with strong velocity-weakening friction. Geophys. J. Int. **179**(3), 1831–1858 (2009). https://doi.org/10.1111/j.1365-246X.2009.04387.x

Rojas, O., Otero, B., Castillo, J., Day, S.: Low dispersive modeling of Rayleigh waves on partly staggered grids. Comput. Geosci. (2014). https://doi.org/10.1007/s10596-013-9380-0

Rojas, O.J., Spa, C., Puente, J.: High-order leapfrog and rapid expansion time integrations on staggered finite difference wave simulations, vol. 2017, no. 1, pp. 1–5 (2017). https://doi.org/10.3997/2214-4609.201700521

Sethi, H., Shragge, J., Tsvankin, I.: Mimetic finite-difference coupled-domain solver for anisotropic media. Geophysics **86**(1), 45–59 (2021). https://doi.org/10.1190/geo2020-0092.1

Sethi, H., Shragge, J., Tsvankin, I.: Tensorial elastodynamics for coupled acoustic/elastic anisotropic media: incorporating bathymetry. Geophys. J. Int. **228**(2), 999–1014 (2022). https://doi.org/10.1093/gji/ggab374

Shragge, J., Tapley, B.: Solving the tensorial 3D acoustic wave equation: a mimetic finite-difference time-domain approach. Geophysics **82**(4), 183–196 (2017). https://doi.org/10.1190/geo2016-0691.1

Solano Feo, F.: Un esquema mimético en diferencias finitas para la ecuación de onda acústica. Master's Thesis, Universidad Central de Venezuela (2017)

Solano-Feo, F., Guevara-Jordan, J.M., Rojas, O., Otero, B., Rodriguez, R.: A new mimetic scheme for the acoustic wave equation. J. Comput. Appl. Math. **295**, 2–12 (2016). https://doi.org/10.1016/j.cam.2015.09.037. (**VIII Pan-American Workshop in Applied and Computational Mathematics**)

Stein, S., Wysession, M.: An Introduction to Seismology, Earthquakes, and Earth Structure, p. 515. Blackwell Publishing, Hoboken (2009)

Strikwerda, J.C.: Finite Dfference Schemes and Partial Differential Equations , 2nd edn., p. 427. SIAM, Philadelphia (2004). https://doi.org/10.1137/1.9780898717938

Authors and Affiliations

Otilio Rojas[1,2] · Larry Mendoza[3] · Beatriz Otero[4] · Jorge Villamizar[5,6] · Giovanni Calderón[6,7] · Jose E. Castillo[8] · Guillermo Miranda[2]

Otilio Rojas
otilio.rojas@bsc.es

Larry Mendoza
prodimat@gmail.com

Jorge Villamizar
jorge@uis.edu.co

Giovanni Calderón
giovanni.calderon@correo.uis.edu.co

Jose E. Castillo
jcastillo@sdsu.edu

Guillermo Miranda
unigrav7@gmail.com

[1] CASE, Barcelona Supercomputing Center, Plaça Eusebi Güell, 1-3, 08034 Barcelona, Cataluña, Spain

[2] Facultad de Ciencias, Universidad Central de Venezuela, Av. Los Ilustres, Caracas 1050, Distrito Federal, Venezuela

[3] Facultad de Ingeniería, Universidad Central de Venezuela, Caracas 1050, Venezuela

[4] Computer Architecture Department, Universitat Politècnica de Catalunya, C/Jordi Girona 1-3, 08034 Barcelona, Cataluña, Spain

[5] Facultad de Ingeniería, Universidad de Los Andes, Mérida, Venezuela

[6] Escuela de Matemáticas, Universidad Industrial de Santander, Bucaramanga, Santander, Colombia

[7] Facultad de Ciencias, Universidad de Los Andes, Mérida, Venezuela

[8] Computational Science Research Center, San Diego State University, San Diego, CA, USA